Effect of Strakes on the Autorotational Characteristics of Noncircular Cylinders

B. N. Pamadi* and H. S. Pordal†
Indian Institute of Technology, Bombay, India

An experimental investigation is conducted to evaluate the effects of windward strakes on the autorotational characteristics of a typical noncircular cylinder. The results indicate that autorotational speeds are very sensitive to strake height and, more particularly, to their location. Reductions in autorotational speeds by as much as 75% were obtained for a strake height of $h/b_0 = 0.3$ located at $r/b_0 = 0.2$. Exploratory two-dimensional pressure measurements indicated that the strakes themselves develop significant, pro- or antiautorotational side forces depending on their location. A strip theory analysis showed that a reduction in ϕ_c, is mainly responsible for this phenomenon.

Nomenclature

b_0 = width of the model
C_n = moment coefficient about axis of rotation, = moment/$\frac{1}{2}\rho V^2 b_0 \ell^2$
C_p = pressure coefficient, = $(p-p_\infty)/\frac{1}{2}\rho V^2$
C_y = sectional side force coefficient, = side force per unit length/$\frac{1}{2}\rho V^2 b_0$
C_{y0} = sectional side force coefficient of the basic cross-sectional shape only
C_{ym} = maximum positive value of C_y
C_{ys} = net side force on strake assembly, $C_{ys1} + C_{ys2}$
C_{ys1} = side force coefficient of left strake
C_{ys2} = side force coefficient of right strake
h = strake height
ℓ = length of the autorotation model
ℓ_1 = axial distance between the leading edge of the autorotation model and its center of gravity
ℓ_1' = ℓ_1/ℓ
ℓ_2 = axial distance between the center of gravity and trailing edge of the autorotation model
ℓ_2' = ℓ_2/ℓ
N = moment about axis of rotation
p = pressure
r = distance measured along the bottom surface from corner to strake location (Fig. 3)
x = coordinate measured from center of gravity along autorotation model axis (Fig. A1)
V = freestream velocity
α = angle of attack
ρ = density of air
η = $(\ell_1 - x)/\ell$
ϕ = cross-flow angle
ϕ_c = value of ϕ when $C_y = 0$
ω = $\Omega\ell/2V$
ω_0 = autorotational speed
Ω = angular velocity

Subscript
∞ = freestream

Received Feb. 10, 1986; revision received Oct. 12, 1986.

*Professor, Aeronautical Engineering Department. Member AIAA.
†Student, Aeronautical Engineering Department (presently Graduate Student, University of Cincinnati, Cincinnati, OH).

Introduction

ON a spinning airplane, the fuselage operates at high angles of attack and its cross sections experience a varying degree of sideslip (Fig. 1a). This cross flow gives rise to side force and yawing moments about the center of gravity. The local side force variation with cross-flow angle can be of two types as shown in Fig. 1b. The variation of type I, where the side force is positive for some range of positive cross-flow angles ($0 < \phi < \phi_c$), leads to instability and autorotation.[1,2] On the other hand, a fuselage having the sectional side force characteristics of type II resists any disturbance in rotation and is stable.

The side force characteristics of the airplane fuselage depend on cross-sectional geometry and Reynolds number.[3] Noncircular cross sections with sharp bottom corners and rounded top surfaces generally produce prospin or autorotative yawing moments.[4-6] Having such a cross-sectional shape, particularly in the aft region, can cause the airplane to be more autorotative. On the other hand, noncircular cross-sectional bodies with well-rounded bottom surfaces are less susceptible to instability and autorotation. The influence of the Reynolds number is also somewhat different in these two cases. For noncircular cross sections with sharp bottom (windward) corners, the primary flow separation points are always fixed at the sharp corners. But the Reynolds number may still have an influence on the location of flow reattachment and secondary separation points. In this manner, the side force characteristics of sections with sharp bottom corners and a rounded top will experience some degree of dependence on the Reynolds number. For the well-rounded cross sections, the Reynolds number will have a significant effect on the primary flow separation point itself and thus the side force characteristics will have appreciable dependence on the Reynolds number.

The autorotational or prospin behavior of an airplane fuselage can be altered by minor modifications to the airframe. One such example is the installation of strakes on the underside of the fuselage. In Ref. 7, the strakes mounted on the bottom of the fuselage were found to alter the spin behavior of the model of a light general aviation airplane. In this case, the strakes were found to be effective in slowing the spin rate and eliminating the flat spin mode of the model. However, the same strakes tested on the full-scale airplane are not found to be as effective in eliminating the flat spin.

In this paper, an experimental investigation is conducted to systematically explore the effects of underside strakes on the autorotational characteristics of noncircular cylinders through single-degree-of-freedom, free-to-roll tests in a low-speed wind tunnel. The noncircular cross-sectional shape selected for this study is the same as the aft fuselage geometry of the light

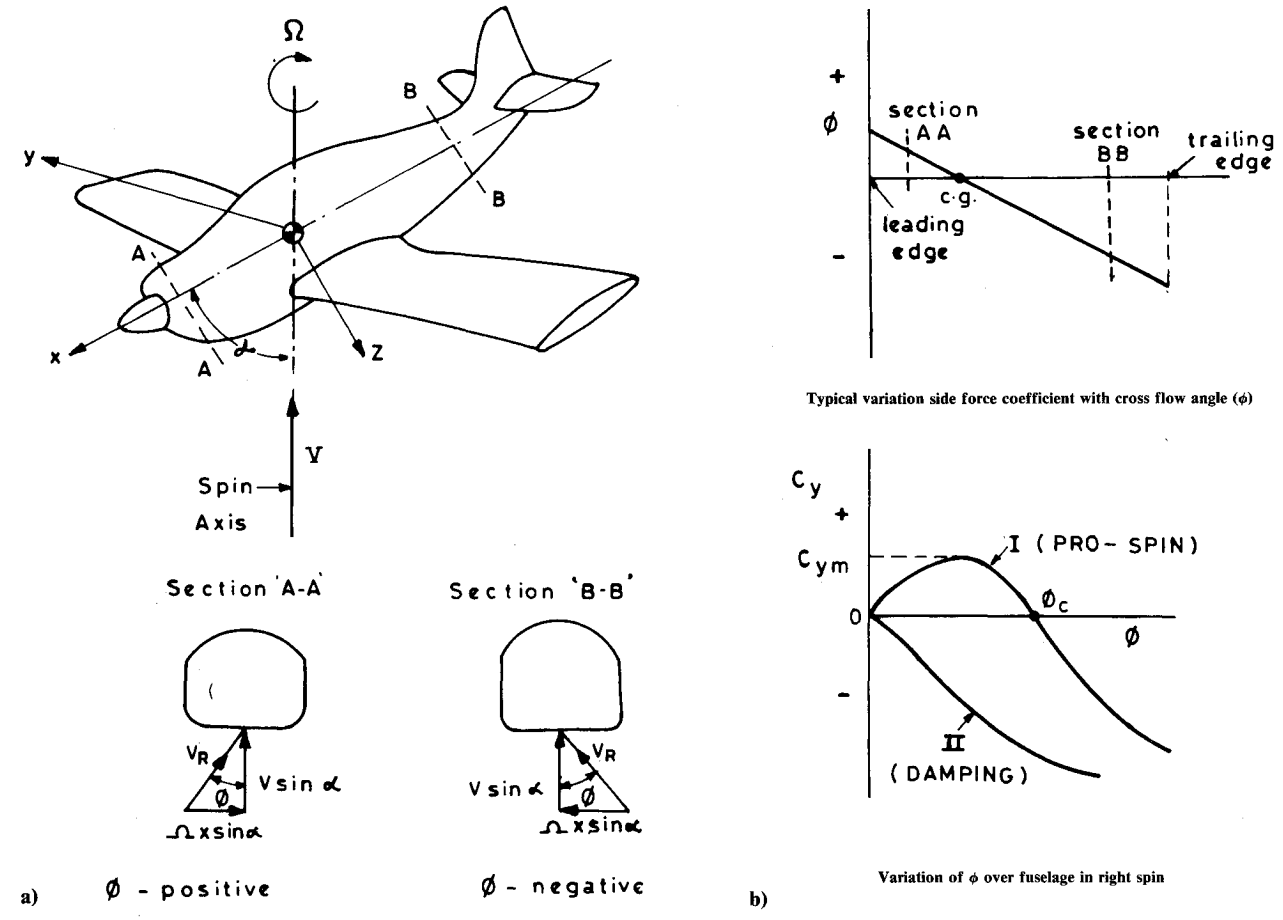

Fig. 1 Schematic diagram of a spinning airplane and cross flow over a fuselage.

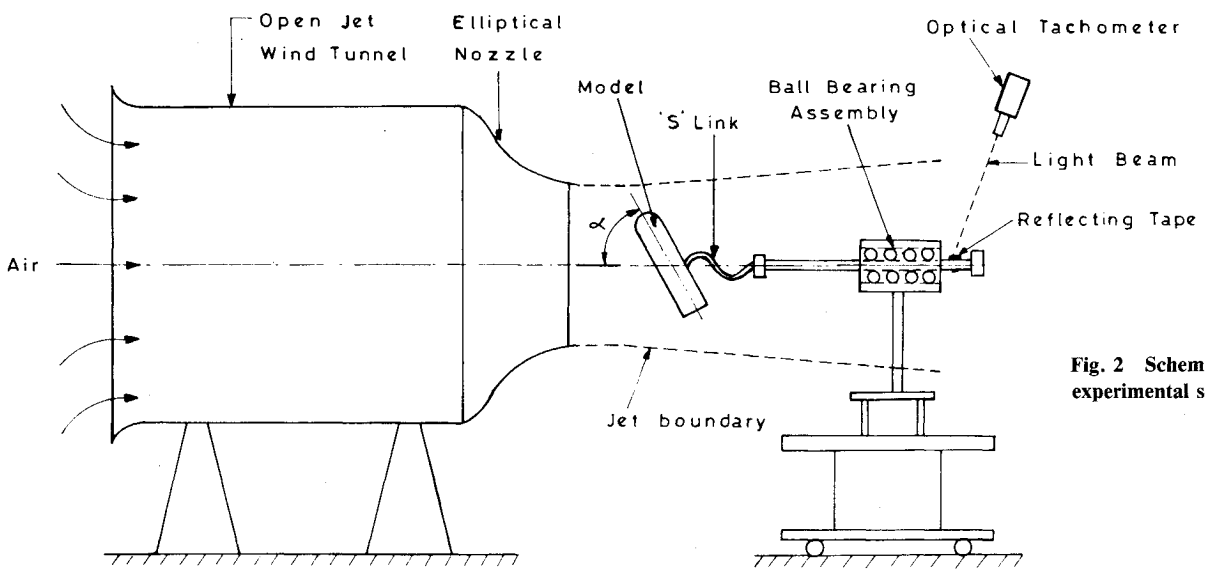

Fig. 2 Schematic diagram of experimental setup.

general aviation airplane used in the investigation of Ref. 7. Full-length strakes of various heights were mounted on the underside of the model in different positions and the corresponding autorotational speeds were measured. It is found that the strake height and, more particularly, the strake location have a strong influence on the autorotational speed of the model. Extensive two-dimensional pressure distribution tests for some selected strake configurations were performed to identify the flow mechanism responsible for the change in the autorotational characteristics due to strakes. A simple analysis based on strip theory is presented to describe quantitatively the effect of strakes in modifying the autorotational behavior of the model.

Experimental Methods

Autorotation Tests

These experiments were conducted in an open-jet, low-speed wind tunnel facility. The nozzle exit cross section of this tunnel is elliptical with major and minor axes measuring, respectively, 76 and 35 cm (30 and 13 in.). The maximum airspeed of this facility is 35 m/s (115 ft/s). A schematic arrangement of the setup is presented in Fig. 2.

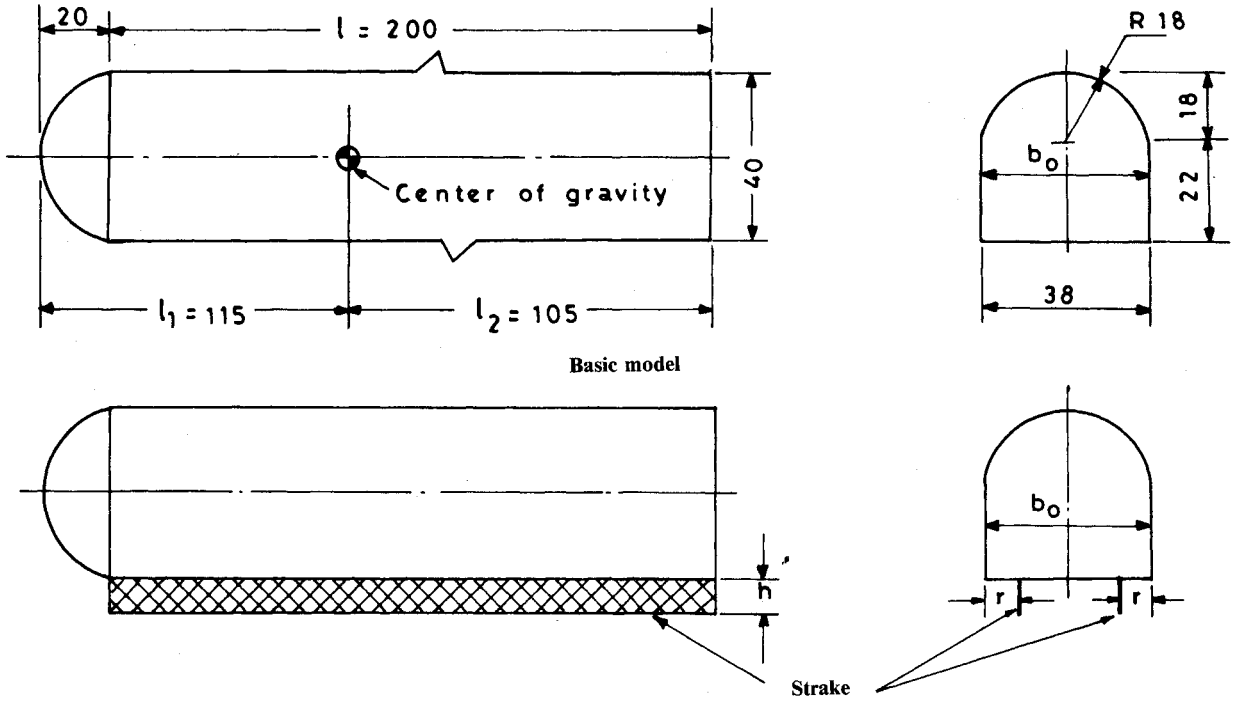

a) Autorotation test model.

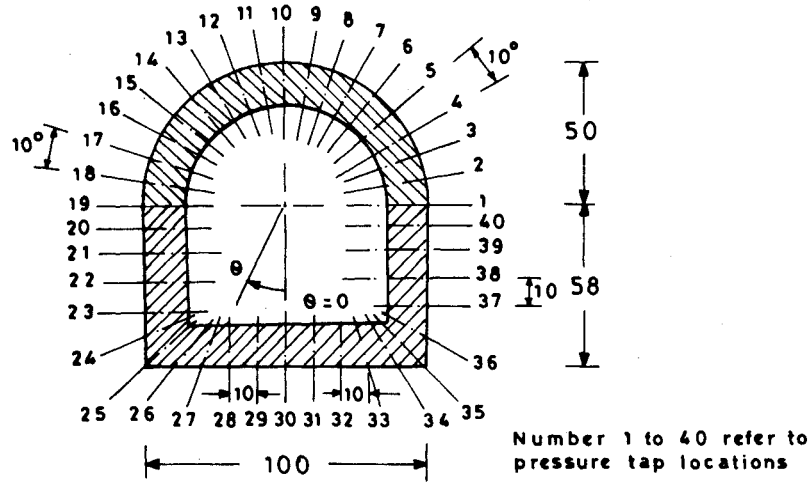

b) Two dimensional pressure test model (all dimensions in mm).

Fig. 3 Test models.

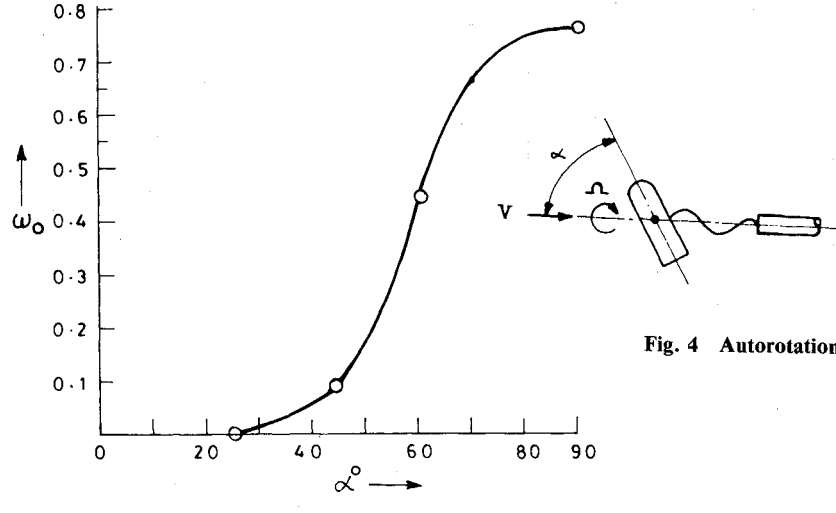

Fig. 4 Autorotational speeds of basic model.

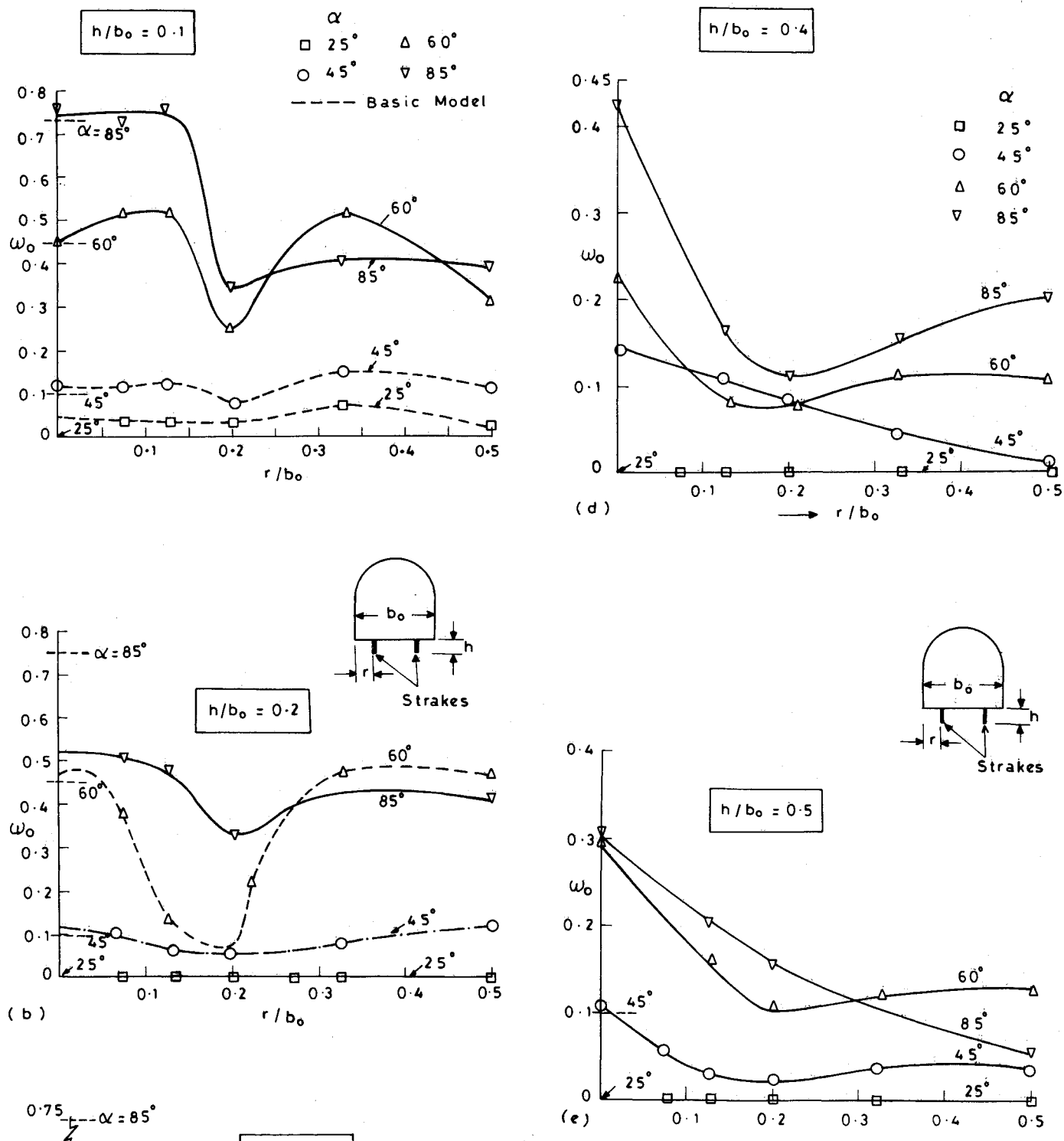

Fig. 5 Effect of strakes on autorotational speeds.

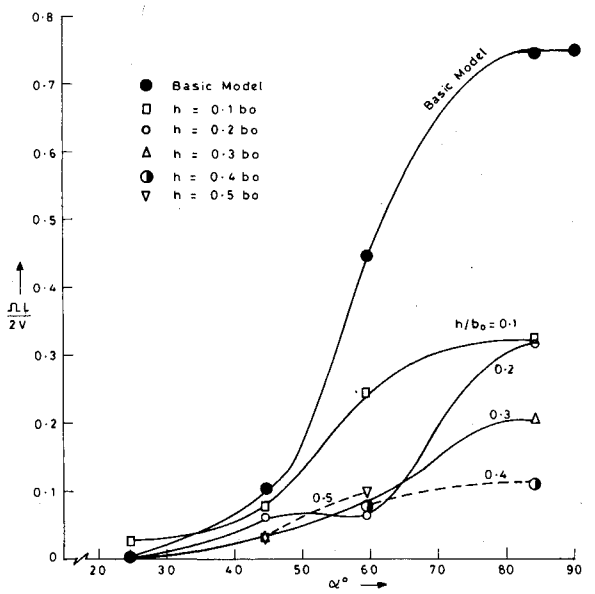

Fig. 6 Variation of minimum autorotational speeds (at $r/b_0 = 0.2$) with angle of attack.

The test models were mounted on a shaft housed in a ball bearing assembly and were free to rotate about the wind axis. The model was attached to the shaft through an S-shaped linkage designed to give a specified angle of attack α to the test model. Four such linkages were fabricated for angles of attack of 25, 45, 60, and 85 deg. An additional arrangement was made for $\alpha = 90$ deg to measure the autorotational speed of the basic model. The models were so mounted that their center of gravity fell on the axis of rotation and were thus statically balanced. However, the assembly of model and S-linkage needed to be balanced. For this purpose, small weights were attached to the shaft at appropriate locations. The autorotational speeds were measured by a noncontact, optical-type digital tachometer.

The geometry of the test models and strake configurations is presented in Fig. 3a. Strakes of various heights ranging from $h/b_0 = 0.1$–0.5 were employed in the present investigation. The strakes were positioned on the bottom side at different locations with r/b_0 varying at 0–0.5. A hemispherical nose shape was smoothly blended to the noncircular section of the model. All of the models were fabricated out of balsa wood and given smooth surface finishes. The strakes were also cut out of thin balsa wood and attached to the model with adhesive tape.

To begin with (wind off), the test model was positioned in the uniform velocity zone of the jet and held stationary at a given angle of attack. The wind tunnel was then started and the model given a slight prerotation. If the model is capable of autorotating, it will quickly accelerate and attain a stable autorotational speed. On the other hand, if the model is not of an autorotational type, the imparted disturbance quickly dies out and the model returns to its initial stationary position.

Pressure Distribution Tests

These tests were carried out in a 60 × 60 cm (23.6 × 23.6 in.) low-speed, closed-jet, open-circuit wind tunnel having a velocity range up to 35 m/s. A test model, having an identical cross-sectional shape as the main body of autorotational model, was constructed from well-seasoned teak wood and polished to produce a smooth surface finish. The test cylinder spanned the horizontal dimension of the wind tunnel test section. The orifice locations at which the pressures were measured are indicated in Fig. 3b. In all, there were 40 orifices located at the midplane cross section of the test cylinder. Some additional orifices at two other equidistant locations on either side of the midplane were also installed to continuously monitor the existance of a true, two-dimensional flow over the model. The cross flow angle ϕ was varied in steps of 5 deg from 0 to ±90 deg.

Pressure distribution was measured for the basic model (no strakes) and for strakes of heights $h/b_0 = 0.1$ and 0.2. For $h/b_0 = 0.1$, extensive pressure measurements were made at regular intervals ($\Delta r/b_0 = 0.1$) for $r/b_0 = 0$–0.5. However, for the strake $h/b_0 = 0.2$, pressure measurements were made only for $r/b_0 = 0$, 0.1, 0.2, 0.35, and 0.5. The pressure over the strakes was not directly measured, as the orifices were not installed on the strakes. Instead, the pressure difference across the strakes was determined by the pressures on the model in the immediate neighborhood of either side of the strakes.

The Reynolds number was around 10^5 in both the single degree-of-freedom, free-to-roll, and two-dimensional pressure distribution tests.

Results and Discussion

Autorotational Characteristics

In Fig. 4, the recorded autorotational speeds for the basic model are presented. The measurements for various strake configurations are given in Figs. 5 and 6.

The autorotational speed ω_0 of the basic model increases rapidly from a value close to zero at $\alpha = 25$ deg to a maximum of 0.75 at $\alpha = 85/90$ deg. At a freestream velocity of 20 m/s, the value $\omega_0 = 0.75$ corresponds to 1300 rpm. The installation of strakes has a marked influence on ω_0 (Fig. 5), particularly at higher angles of attack.

From Fig. 5, we observe that, as the strakes are moved inward ($r > 0$), ω_0 starts dropping. This decrease becomes pronounced for $0.1 < r/b_0 \leq 0.2$ and ω_0 assumes a minimum value around $r/b_0 = 0.2$. This interesting phenomenon happens in all but two cases, namely $h/b_0 = 0.4$ at $\alpha = 45$ deg and $h/b_0 = 0.5$ at $\alpha = 85$ deg, where ω_0 monotonically decreases toward $r/b_0 = 0.5$, as shown in Figs. 5d and 5e. These two cases are regarded as exceptions to the general observations of this study. At this point, the reasons for this discrepancy are not clear. As the strakes are moved further inward, ω_0 starts rising again. However, the minimum values of ω_0 at $r/b_0 = 0.2$ are also found to be dependent on the strake height.

The minimum values of ω_0 recorded at $r/b_0 = 0.2$ are plotted in Fig. 6 as a function of α and h/b_0. We notice that very large reductions in ω_0 are obtained for strake heights of $h/b_0 = 0.3$, 0.4, and 0.5, particularly at higher angles of attack. Although strake heights of $h/b_0 = 0.4$ and 0.5 display slightly lower values in ω_0 than $h/b_0 = 0.3$, the difference is not substantial enough (except at $\alpha = 85$ deg) to justify a higher strake height than $h/b_0 = 0.3$. Therefore, it can be surmised that the strake configuration of $h/b_0 = 0.3$ located at $r/b_0 = 0.2$ produces the best overall results for the subject noncircular cross section in terms of reduction in ω_0. The values of ω_0 for this particular strake geometry are only about 25% of the basic model. Therefore, this strake configuration should significantly improve the spin behavior of the corresponding light general aviation airplane model.[7]

Two-Dimensional Side Force Characteristics

The above discussion indicates that the effect of strakes on the autorotational characteristics of the subject noncircular cylinder are quite similar for all of the strake heights employed in the present study. In view of this observation, only two strake heights, $h/b_0 = 0.1$ and 0.2, were chosen for detail surface pressure measurements and evaluation of side force characteristics by an integration of measured pressure data. In Fig. 7, typical pressure distributions (part b) and side force coefficients (part c) for the basic model (no strakes) are presented. In part b of Figs. 8–13, the pressure distribution is presented for the strake configuration $h/b_0 = 0.1$ for $r/b_0 = 0$–0.5. The pressure variation over the model for $h/b_0 = 0.2$ is quite similar and therefore details of these data are not given here. Instead, the parameters C_{ym} and ϕ_c, which in a way characterize the positive loop of $C_y - \phi$ curve, are in-

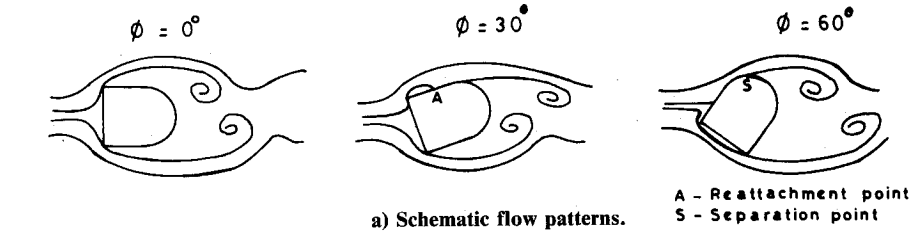

a) Schematic flow patterns.

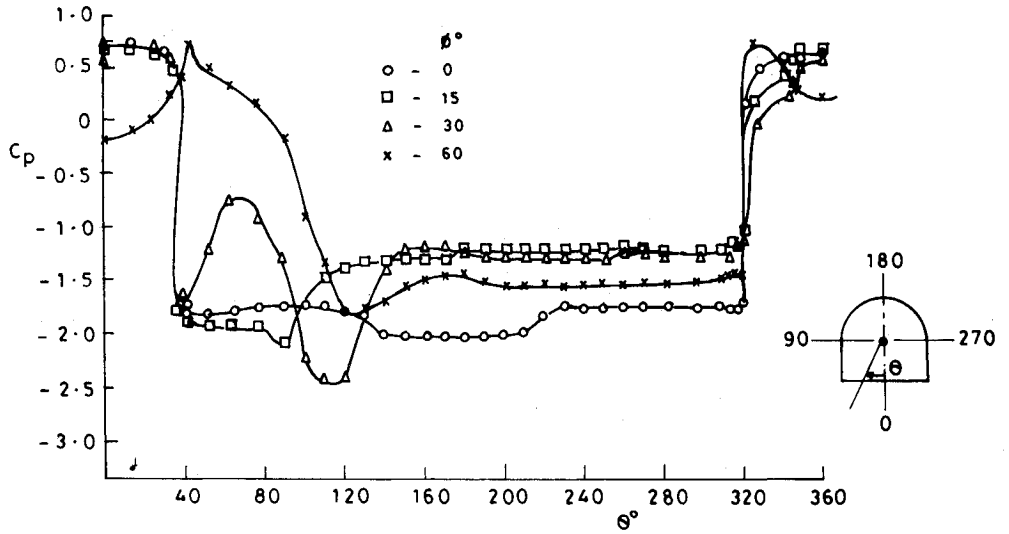

b) Pressure distribution.

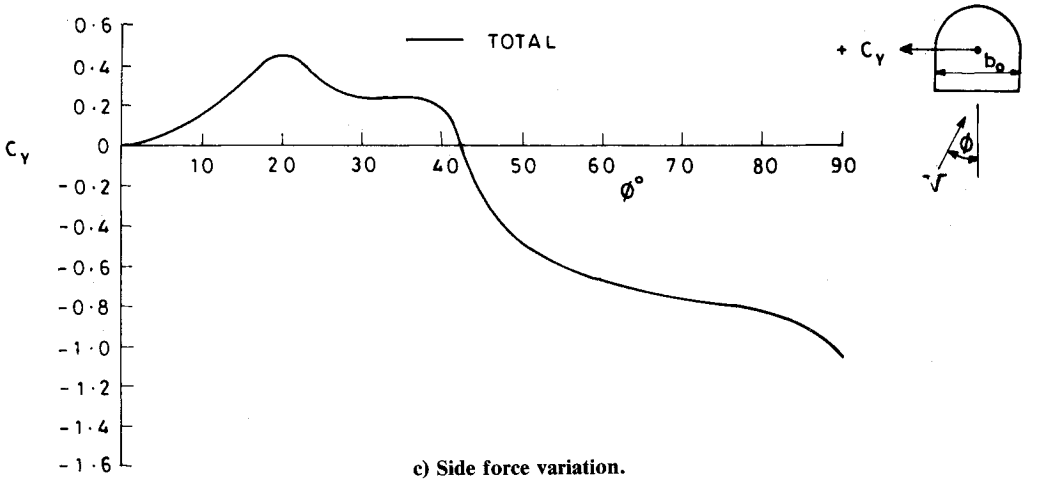

c) Side force variation.

Fig. 7 Two-dimensional flow characteristics of basic model.

cluded in Fig. 14, along with the corresponding data for $h/b_0 = 0.1$.

The surface pressure distribution for typical crossflow angles of $\phi = 0$, 15, 30, and 60 deg are presented as a variation of pressure coefficient C_p with angle θ. The angle θ is measured clockwise from the axis of the model, with $\theta = 0$ located on the bottom side as shown in these figures. The pressure C_p and force data C_y are corrected for wind tunnel blockage effects. Based on the measured surface pressure data, schematic flow patterns are developed and are presented in part a of Figs. 7–13.

The side force on the model can be divided into two parts,

$$C_y = C_{y0} + C_{ys}$$

where C_y is the total side force coefficient, C_{y0} the contribution of the basic shape (strakes excluded) to C_y, only and C_{ys} the net side force coefficient on strake assembly ($= C_{ys1} + C_{ys2}$).

The side forces over the strakes, C_{ys1} (windward) and C_{ys2} (leeward), are estimated to be

$$C_{ys1,2} = h/b_0 \cdot \Delta C_{p1,2}$$

where $\Delta C_{p1,2}$ represents the pressure differential across the strakes.

It should be noted that C_{y0} incorporates the influence of strakes on the pressure distribution over the basic noncircular cross section and C_{y0} is not equal to the side force coefficient of the basic model.

Basic Model

As shown in the schematic sketch of the flow pattern (Fig. 7a) at $\phi = 0$, the flow separates from the sharp bottom (wind-

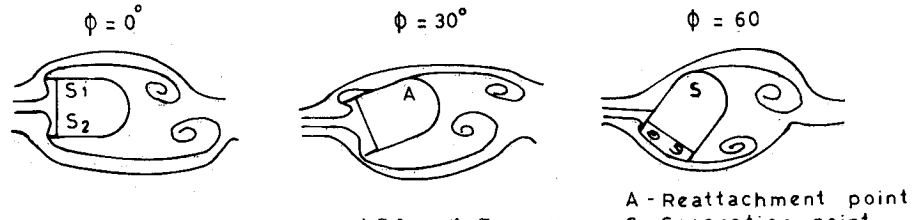

a) Schematic flow patterns.

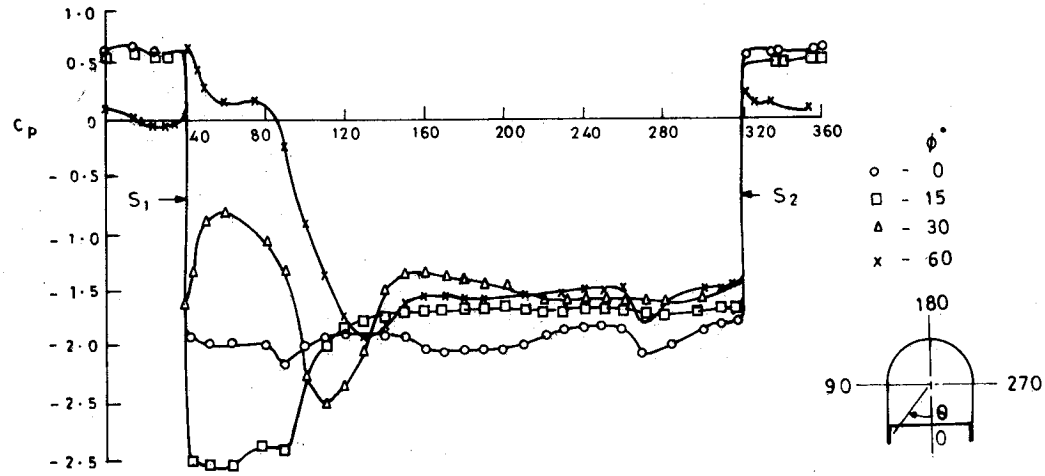

b) Pressure distribution.

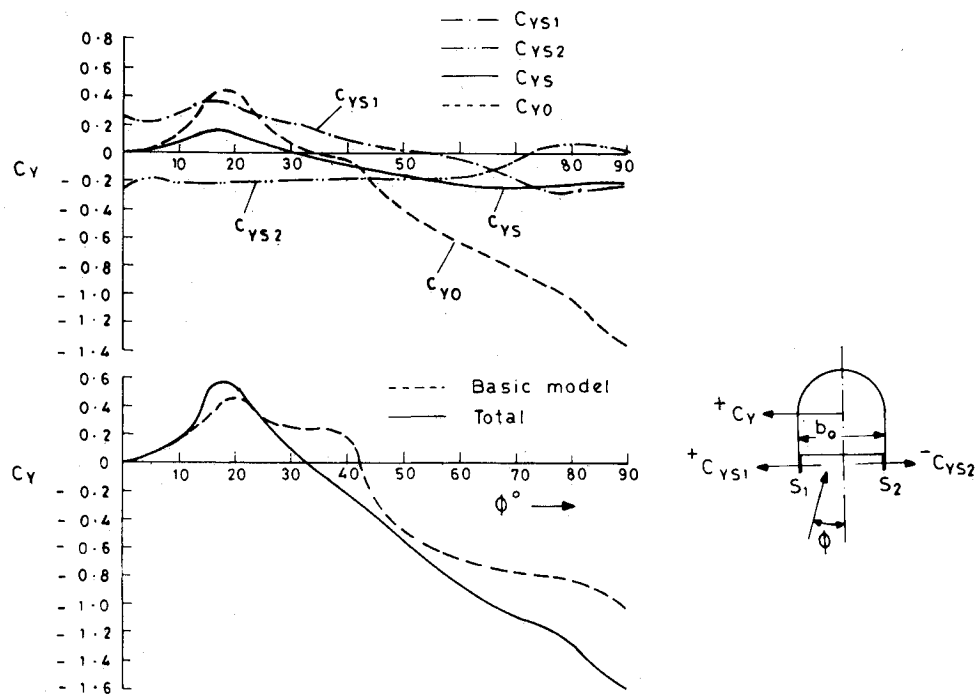

c) Side force variation.

Fig. 8 Two-dimensional flow characteristics for $r/b_0 = 0$ and $h/b_0 = 0.1$.

ward) corners and rolls up into a pair of alternating vortices. In the Reynolds number range of 10^4–10^5, such bluff bodies are known[9] to give rise to the phenomenon of vortex shedding with a Strouhal number (fb_0/V) around 0.12–0.14, where f is the frequency of vortex shedding. Although a direct study of this phenomenon was beyond the scope of this work, the fluctuating pressures observed during experimentation were evidence to this fact. It should be noted that, in this work, only time-averaged pressures were measured.

When the cross flow angle increases (either positively or negatively) to a value around 15 deg, the flow separated from the windward corner reattaches to the model (point A) as shown in Fig. 7a. This value of $\phi = 15$ deg is in good agreement with Obasaju,[9] who gives $\phi = 13.5$ for a square cylinder. It is quite possible that this value of ϕ is influenced by the Reynolds number and turbulence intensity, as discussed in Ref. 9. After reattachment, the flow follows the model contour for some distance and thereby gives rise to larger suction

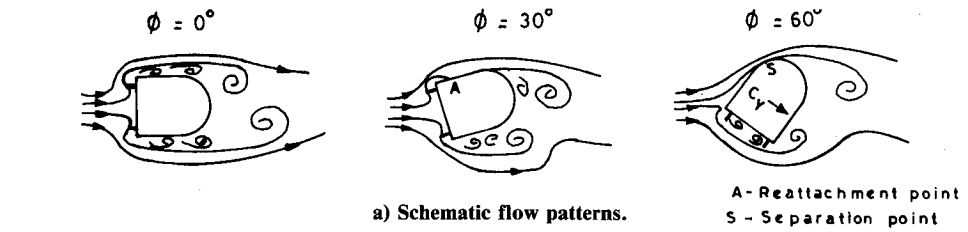

a) Schematic flow patterns.

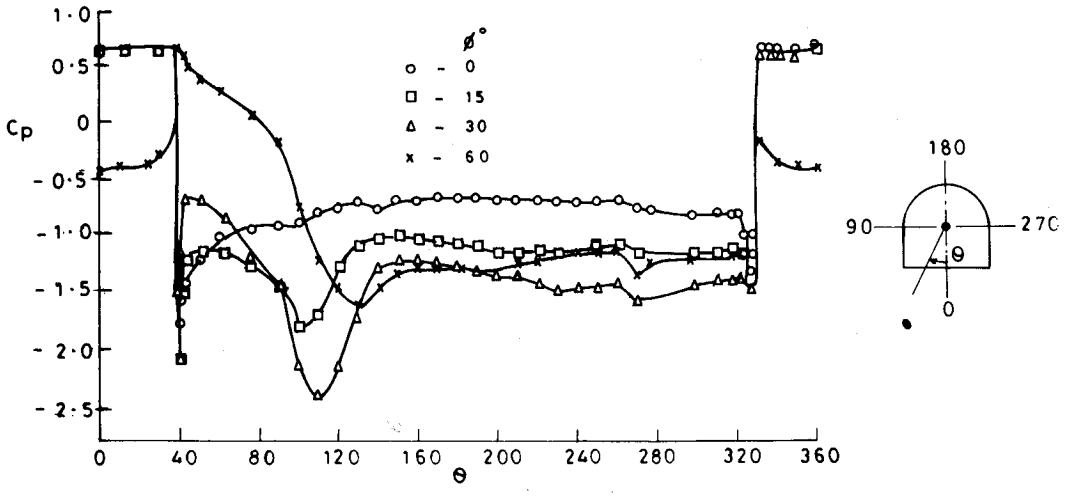

b) Pressure distribution.

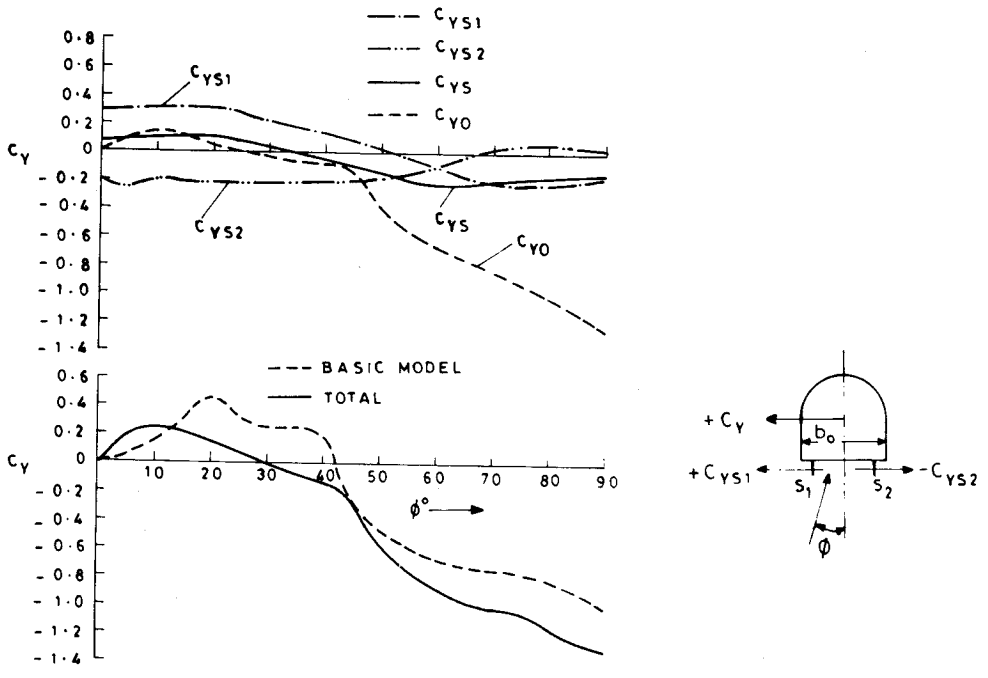

c) Side force variation.

Fig. 9 Two-dimensional flow characteristics for $r/b_0 = 0.1$ and $h/b_0 = 0.1$.

pressures. Eventually, the reattached flow separates once again around $\theta = 160$ deg (point S) and this is followed by a significant pressure rise characteristic of turbulent separation. This suggests that the flow transition occurred prior to separation. This difference in the flow pattern leads to higher negative pressures on the windward face and results in a positive side force at low and moderate values of ϕ. As ϕ increases, positive pressures occur on the windward side and the side force starts decreasing, becoming zero at $\phi = \phi_c$. For still higher values of ϕ, the side force becomes negative (damping).

Strake Configurations

For corner strakes ($r = 0$) (Fig. 8a) at small cross flow angles, the flow turns more sharply at the windward (left) corner compared to the leeward corner. This action of the fluid flow generates relatively higher negative pressures (Fig. 8b) on the outer surface of the left strake compared to the right strake. As a result, a net positive side force (Fig. 8c) acts on the strake assembly, which encourages the autorotational tendency. The other features of the flow are quite similar to the basic model. With an increase in ϕ, the stagnation point

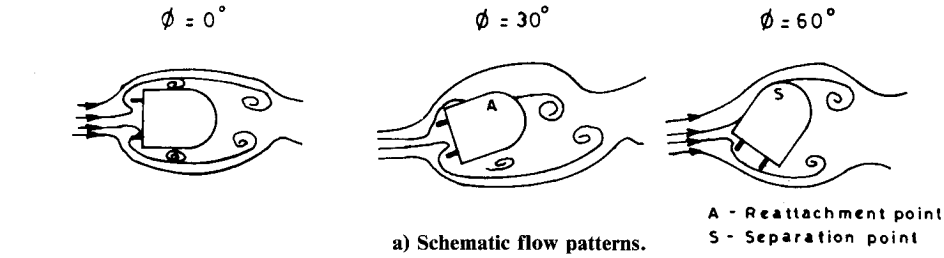

a) Schematic flow patterns.

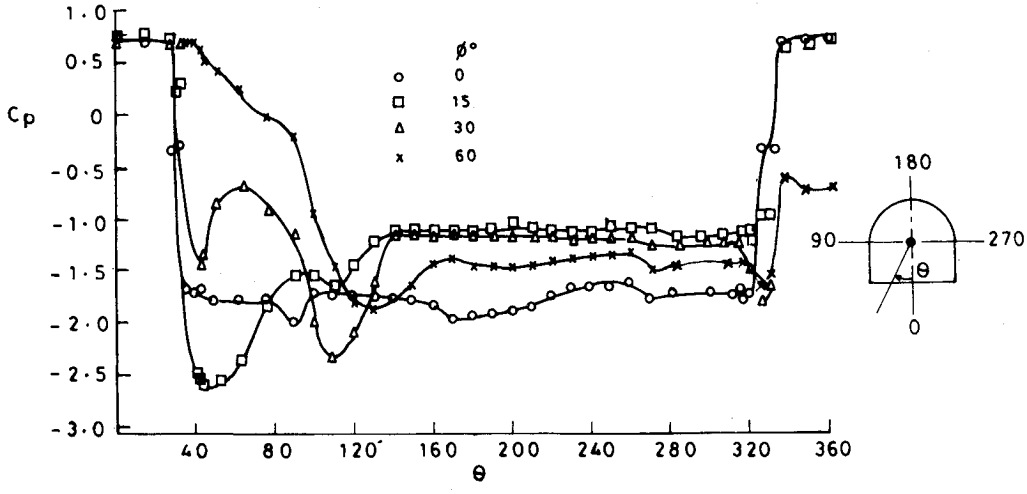

b) Pressure distribution.

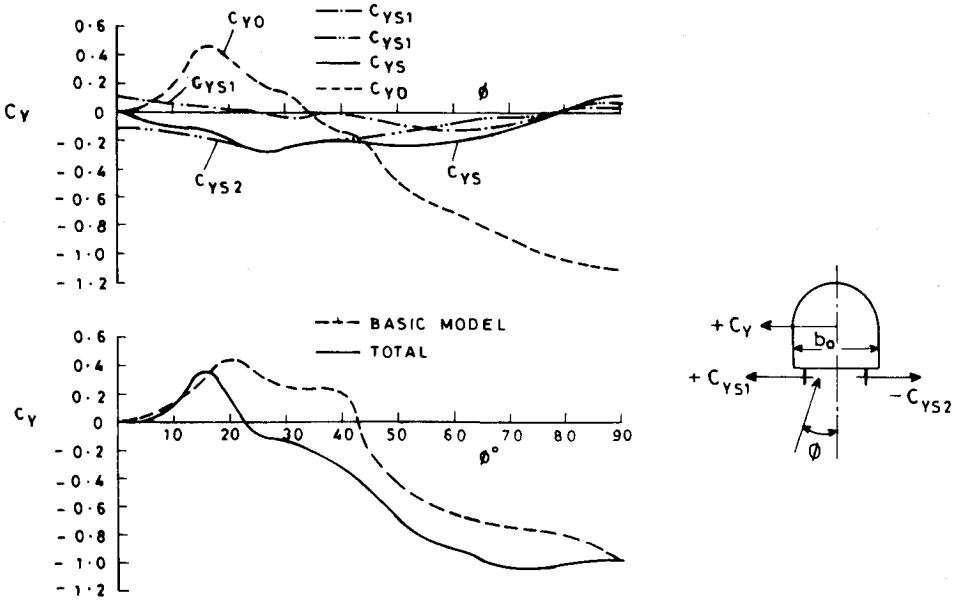

c) Side force variation.

Fig. 10 Two-dimensional flow characteristics for $r/b_0 = 0.2$ and $h/b_0 = 0.1$.

moves on to the windward strake (see Figs. 9a and 9b for $\phi = 60$ deg) and positive pressures occur on the outer side of the windward strake. As a result, the windward strake also generates negative side forces, adding to the negative side force of the leeward strake. Thus, the net side force due to the strake assembly is negative for $\phi > 32$ deg (damping).

When the strakes are located at $r/b_0 = 0.2$, a different flow pattern occurs for low and moderate values of ϕ. The flow does not attempt to negotiate the windward strake, but instead prefers to bend much ahead of the windward strake, as shown in Fig. 10a for $\phi = 30$ deg. This phenomenon greatly suppresses the generation of a large pressure differential across the windward strake (Fig. 10b) and as a result the magnitude of C_{ys1} is much smaller. Over the leeward strake, the flow turns sharply and produces comparatively higher negative side force. So, the net side force over strake assembly C_{ys} becomes negative and opposes the autorotational tendency (Fig. 10c).

For $r/b_0 = 0.3$ (Fig. 11), the flow pattern and side forces are similar in nature to $r/b_0 = 0.2$; however, in comparison, the net side force over strakes C_{ys} is smaller in magnitude.

For the strake location $r/b_0 = 0.4$, the flow pattern changes as shown in Fig. 12. On approaching the strake assembly, the flow turns leeward. This flow pattern generates positive pressures on the upper surface of windward strake S_1 and a negative C_{ys1}. The side force on leeward strake C_{ys2} is always negative. However, the overall pressure differentials and the

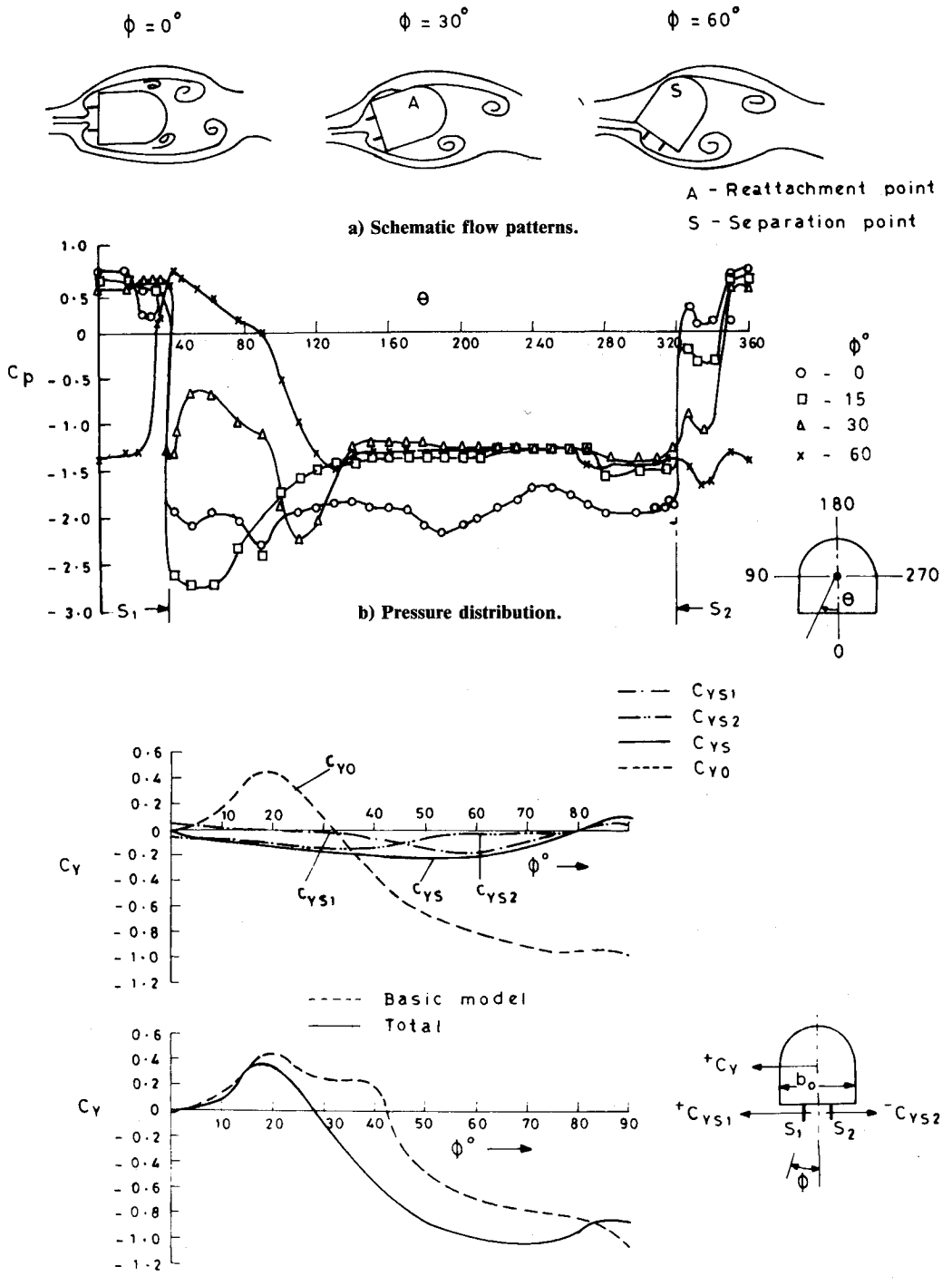

Fig. 11 Two-dimensional flow characteristics for $r/b_0 = 0.3$ and $h/b_0 = 0.1$.

side force C_{ys} are smaller in magnitude compared to $r/b_0 = 0.2$.

With the strakes at the center ($r/b_0 = 0.5$) (Fig. 13), the flow pattern similar to $r/b_0 = 0.4$ and C_{ys} is negative. However, the magnitude of C_{ys} is smaller compared to $r/b_0 = 0.2$.

From the above discussion, we see that the strakes can produce both pro- and antiautorotational side forces depending on their location. This effect can be described in terms of two parameters, C_{ym} and ϕ_c. Here, C_{ym} is the maximum value of sectional side force for a positive value of ϕ (and vice versa for negative ϕ) and ϕ_c is the cross-flow angle when C_y changes sign. These two parameters adequately quantify the positive loop of the $C_y - \phi$ curve, the existence of which causes autorotation. In Fig. 14, C_{ym} and ϕ_c are presented for basic model and various strake configurations as measured from parts c of Figs. 7–13. Also included in Fig. 14 are the data points for $h/b_0 = 0.2$. It is interesting to observe that with strakes, both C_{ym} and ϕ_c are in general much smaller than basic model values (except for $r = 0$). The parameter ϕ_c displays a minimum value at $r/b_0 = 0.2$. It may be recalled that the minimum autorotational speeds occur at this strake location. In order to explore whether the minimum values of ϕ_c and ω_0 have any relation, a simple strip theory similar to that reported in Ref. 8 is developed and is given in the Appendix. The input to this theory is the empirical (measured) values of C_y as functions of ϕ. These values are taken from parts c of

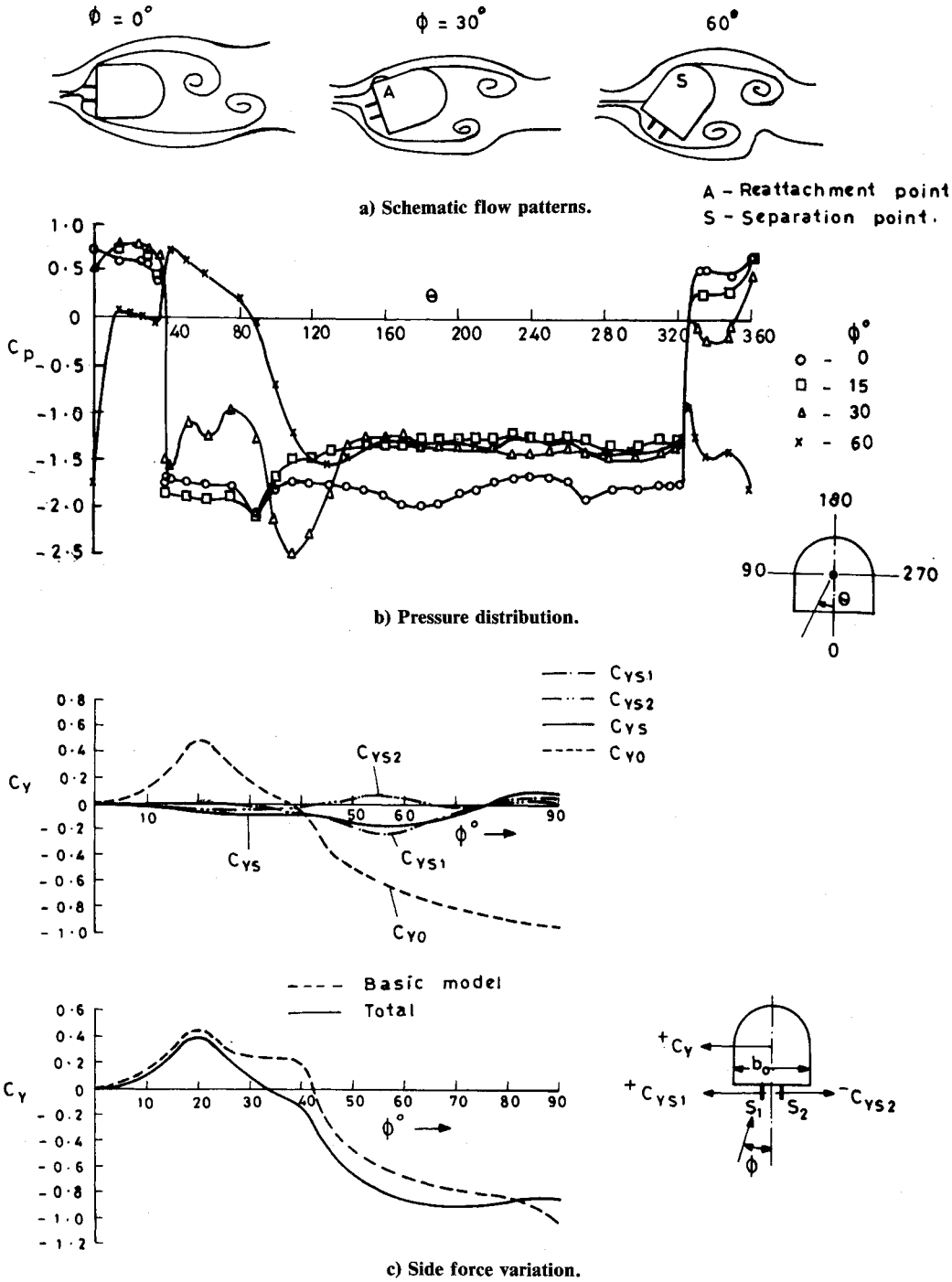

Fig. 12 Two-dimensional flow characteristics for $r/b_0 = 0.4$ and $h/b_0 = 0.1$.

Figs. 8–13 and used in the calculations. The damping effect of the hemispherical nose and the corrections for two-dimensional values of C_y for end effects are ignored here. However, this approximate theory serves as a basis for making a relative comparison of various strake locations.

The results of strip theory calculations are presented in Fig. 15 for $\alpha = 60$ deg. A similar result was obtained at other angles of attack. It is interesting to note that ω_0 happens to be minimum for $r/b_0 = 0.20$. Thus, the reduction in ϕ_c appears to have a direct effect on ω_0. However, a decrease in C_{ym} results in smaller autorotative or prospin moments, but will not substantially affect ω_0. Therefore, the phenomenon responsible for the occurence of minimum autorotational speeds when the strakes are located at $r/b_0 = 0.2$ is found to be the existence of large damping side forces generated by strakes. This effect can be expressed in terms of the reduction in the parameter ϕ_c as demonstrated here.

Effect of Reynolds Number

The flow pattern giving rise to the autorotational side force over the model is based on the separation on the lee side and the reattachment of the flow separated from the windward corner back to the model surface. As discussed earlier, this flow pattern leads to differential pressures over the model and an autorotative side force comes into existence. The Reynolds number can have a significant influence on the location of reattachment point and, thereby, on the sectional side force. However, as far as the strakes are concerned, the pressure differentials and side forces on strakes appear to be primarily dictated by flow directions rather than the Reynolds number.

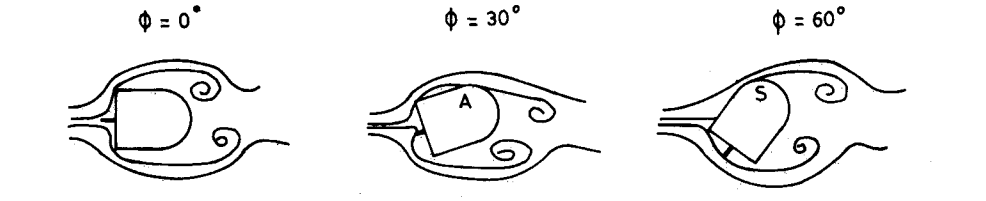

a) Schematic flow patterns.

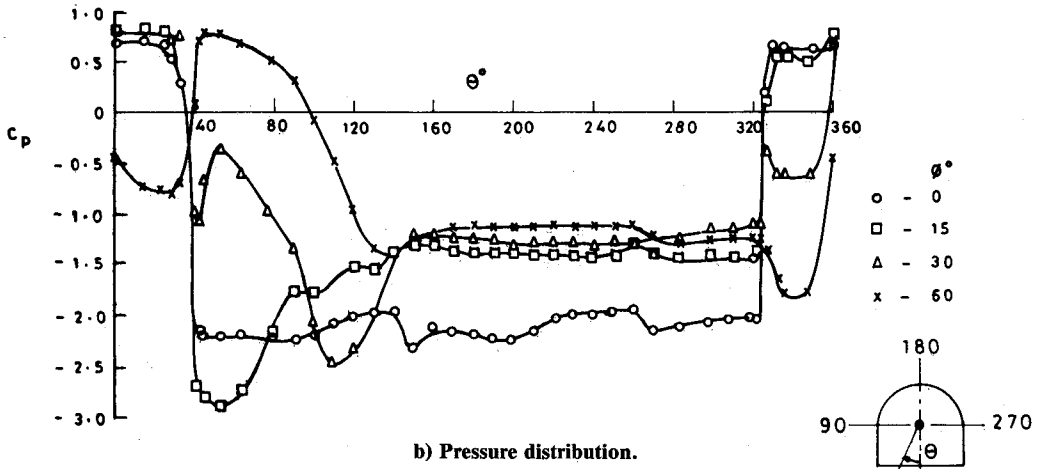

b) Pressure distribution.

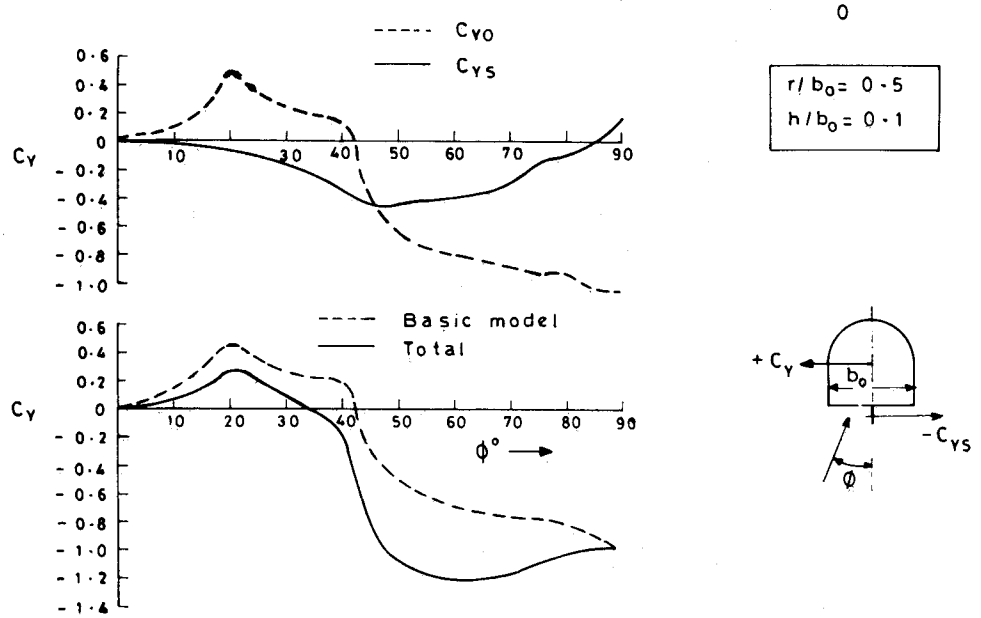

c) Side force variation.

Fig. 13 Two-dimensional flow characteristics for $r/b_0 = 0.5$ and $h/b_0 = 0.1$.

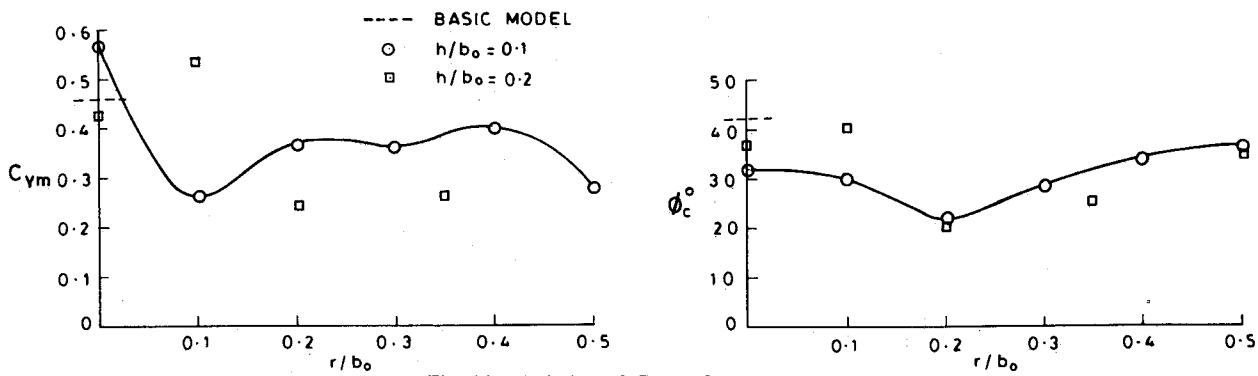

Fig. 14 Variation of C_{ym} and ϕ_c with r/b_0.

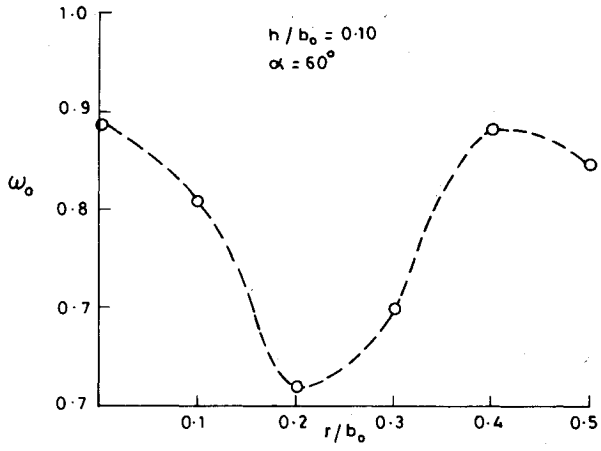

Fig. 15 Variation of ω_0 with r/b_0 (strip theory calculations).

Thus, the overall effect of the Reynolds number on the model with strake depends on which of the above two phenomena dominate. In other words, a particular strake height location, which may have an antiautorotational or spin effect on the model, may not be as effective on the full-scale aircraft, as observed in Ref. 7. Here, the first effect, i.e., the influence of the Reynolds number on the location of the reattachment point on the windward face appears to be prominent. On the other hand, a strake configuration such as $h/b_0 = 0.3$ at $r/b_0 = 0.2$, as found here, may have a substantial benefit on the full-scale aircraft of Ref. 7. The damping effect produced by this configuration appears to be primarily dictated by the flow directions over strakes and may mask the Reynolds number effect in the flow reattachment and secondary separations over the windward face. This fact, however, needs further investigation.

Conclusions

An experimental investigation at low (model) Reynolds numbers was conducted to evaluate the effect of strakes on the autorotational characteristics of noncircular cylinders. The cross-sectional shape tested was typical of the aft geometry of a light aircraft fuselage. It is found that large reductions in autorotational speeds are possible by this kind of minor geometrical modification. Maximum reductions in autorotational speed were obtained for a strake location of $r/b_0 = 0.2$. For example, a strake of height $h/b_0 = 0.3$ located at $r/b_0 = 0.2$ gave autorotational speeds that were 25% or even less compared to the basic model.

Extensive two-dimensional pressure distribution tests at low Reynolds numbers were performed to understand the basic flow mechanism leading to the decrease in autorotational speeds. These tests indicated that, depending on their height and particularly their location, the strakes can produce significant pro- or antiautorotational side forces. This effect can be quantified in terms of two parameters, C_{ym} and ϕ_c. A simple strip theory demonstrated that the autorotational speeds are influenced more by parameter ϕ_c and not much by C_{ym}.

The effect of the Reynolds number on the autorotational characteristics of strake configurations was not investigated in this study. The influence of the Reynolds number can be significant and can affect strake characteristics.

Appendix

Let us consider a model mounted on the single-degree-of-freedom, autorotational apparatus (Fig. A1) and rotating steadily at an angular velocity Ω. The cross-flow angle and dynamic pressure at any cross section along with the length of the model are given by

$$\phi = \tan^{-1}\left(\frac{\Omega x}{V}\right) \tag{A1}$$

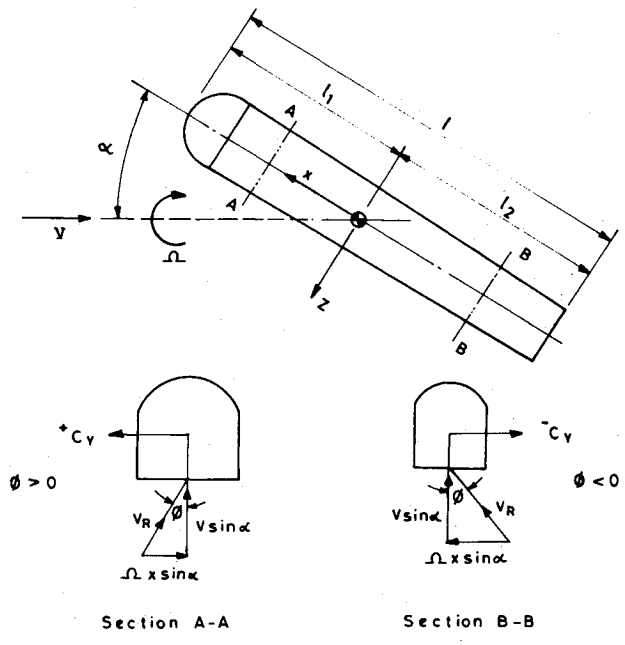

Fig. A1 Schematic diagram of autorotating model.

and

$$q = \tfrac{1}{2}\rho V^2\left[1 + \left(\frac{\Omega x \sin\alpha}{V}\right)^2\right] \tag{A2}$$

For simplicity, the sectional side force is assumed to rise only from viscous cross flow corresponding to $V\sin\alpha$. The potential flow component of C_y is neglected. The moment about the axis of rotation due to a strip of width dx located at a distance x from the center of gravity (Fig. A1) is given by

$$\Delta N = \tfrac{1}{2}\rho V^2\left[1 + \left(\frac{\Omega x \sin\alpha}{V}\right)^2\right] C_y b_0 x \sin\alpha dx \tag{A3}$$

and the local moment coefficient,

$$\Delta C_n = \frac{1}{\ell^2}\left[1 + \left(\frac{\Omega x \sin\alpha}{V}\right)^2\right] C_y x \sin\alpha dx \tag{A4}$$

Let $\eta = (\ell_1 - x)/\ell$, so that $dx = -\ell d\eta$. With $\omega = \Omega\ell/2V$ and $\ell_1' = \ell_{1/\ell}$, we have

$$\phi = \tan^{-1}[2\omega(\ell_1' - \eta)] \tag{A5}$$

and

$$C_n = \sin\alpha \int_0^1 [1 + \{2\omega \sin\alpha(\ell_1' - \eta)\}^2] C_y(\ell_1' - \eta) d\eta \tag{A6}$$

For autorotation, $C_n = 0$. The autorotational speed ω_0 corresponds to the value of ω that satisfies the condition $C_n = 0$.

In the above equations, C_y is a function of ϕ. The two-dimensional test data given in parts c of Figs. 8-13 for various strake configuration were employed in solving Eq. (A6) to find ω_0.

References

[1]Clarkson, M. H., "Auto-rotation of Fuselages," IAS Paper 770, Jan. 1958.

[2]Pamadi, B. N. and Taylor, L. W. Jr., "On the Prediction of Autorotational Characteristics of Light Airplane Fuselages," AIAA Paper 84-2112, 1984.

[3]Polhamus, E. C., "Effects of Flow Incidence and Reynolds Number on Low Speed Aerodynamic Characteristics of Several Noncircular Cylinders with Application to Directional Stability and Spinning," NASA Tech. Rept. R-29, 1959.

[4]Beaurain, L., "General Study of Light Airplane Spin, Aft Fuselage Geometry, Part I," NASA TTF-17446, 1977.

[5]Bihrle, W. Jr. and Bowman J. S., "Influence of Wing, Fuselage and Tail Design on Rotational Flow Aerodynamics beyond the Maximum Lift," *Journal of Aircraft*, Vol. 18, Nov. 1981, pp. 920–925.

[6]Irving, H. B., Batson, A. S., and Warsap, J. H., "The Contribution of Body and Tail of an Aeroplane to the Yawing Moment in a Spin," Aeronautics Dept., N.P.L., Report and Memoranda No. 1689, Nov. 1935.

[7]Burk, S. M., Bowman, J. S., and White, W. L., "Spin Tunnel Investigations of the Spinning Characteristics of Typical Single Engine General Aviation Airplane Designs, Part I: Low Wing Model A: Effects of Tail Modifications," NASA TP-1009, Sept. 1977.

[8]Pamadi, B. N. and Taylor, L. W. Jr., "Estimation of Aerodynamic Forces and Moments on a Steadily Spinning Airplane," *Journal of Aircraft*, Vol. 21, Dec. 1984, pp. 943–954.

[9]Obasaju, E. D., "An Investigation of the Effects of Incidence on the Flow around a Square Section Cylinder," *Aeronautical Quarterly*, Vol. 34, Nov. 1983, pp. 243–259.